Struct Multidisc Optim (2014) 50:489–503
DOI 10.1007/s00158-014-1072-4

INDUSTRIAL APPLICATION

On addressing noise constraints in the design of wind turbine blades

Simão S. Rodrigues · André C. Marta

Received: 28 June 2013 / Revised: 20 January 2014 / Accepted: 14 February 2014 / Published online: 23 March 2014

Abstract Power production from wind energy has been increasing over the past decades, with more areas being used as wind farms and larger wind turbines (WTs) being built. With this development, awareness of the impact of wind energy on the environment and on human health has also raised. There has been a large interest in developing fast turnaround WT blade design frameworks, capable of predicting both aerodynamic and aeroacoustic performance to handle ever stricter noise criteria constraints dictated by site or local authorities. In this work, a blade element momentum theory model is used to predict the aerodynamic performance of a wind turbine, coupled to an empirical aeroacoustic noise model and boundary layer corrections. The aeroacoustic prediction code developed was validated against measurement data of the AOC 15/50 WT and included in an optimization framework using a genetic algorithm. The blade shape was parametrized using NURBS curves for the cross sectional airfoil shapes and Bézier curves for the twist and chord distributions, totaling up to 62 design variables. Two multi-objective optimization cases, both single- and multi-operating point, were performed. Optimal solutions selected from the Pareto fronts are discussed in detail. These solutions ranged from an increase in annual energy production of 15 % to a reduction in noise levels of 9.8 %. It was demonstrated that substantial noise reduction could be obtained at an expense of a minor aerodynamic penalty.

S. S. Rodrigues (✉) · A. C. Marta
Instituto Superior Técnico, Av. Rovisco Pais 1,
1049 Lisboa, Portugal
e-mail: simao.rodrigues@ist.utl.pt

A. C. Marta
e-mail: andre.marta@ist.utl.pt

Keywords Aeroacoustic · Optimization · Wind turbines · NURBS · Genetic algorithms · Pareto front

1 Introduction

For the past few decades, wind energy has seen a big development, with larger wind turbines (WT) being used and more wind farms being constructed. This led to an increase in awareness of the impacts of wind energy in the environment and human health, with many studies being performed on this subject (Stephens et al. 1982; Pedersen and Waye 2004; Colby et al. 2009). While there are no common international noise standards or regulations for sound pressure levels, these are usually regulated by the legislation of each country, which defines maximum noise levels according to time of day and type of area. These limitations to generated noise make it necessary to address the issue early in the design phase of wind turbines.

The main objective of the work presented in this paper was to develop a fast turnaround WT blade design framework that capable of handling noise criteria constraints dictated by a specific customer or site location. That framework should be able to predict both the aerodynamic performance and noise emissions of a WT, with low computational cost, and to optimize user-defined shape parameters of the WT blade geometry to satisfy certain noise and aerodynamic requirements. To accomplish that, a multi-disciplinary and multi-objective optimization framework using low-fidelity prediction codes was developed.

While published work aims at reducing WT noise either by changing the 3D blade planform parameters such as chord and twist distributions (Leloudas 2006) or by optimizing the 2D airfoil shapes (Schepers et al. 2007; Bizzarrini et al. 2011; Coimbra 2012; Göçmen and Özerdem 2012),

little literature exists on the simultaneous optimization of both airfoil shapes and blade parameters. Petrone et al. (2011) presents a similar approach to the one in this paper but taking into account the uncertainty in the parameters and therefore requiring the use of a high performance computing environment.

This paper contains four main sections. In Section 2, a survey of low-fidelity aerodynamic and aeroacoustic models is presented. Section 3 includes the details of the implementation of the aeroacoustic analysis and shape parametrization tools, as well as the optimization framework. This section ends with the validation of the aeroacoustic prediction tool by comparison of numerical with experimental data. Two optimization cases, considering single and multiple operating wind speeds, are presented and discussed in Section 4. Finally, some conclusions and remarks about the work presented can be found in Section 5.

2 Prediction models

In this section, the theoretical background of the aerodynamic and aeroacoustic models is presented and briefly discussed.

2.1 Aerodynamic model

The aerodynamic model, besides predicting the performance of the wind turbine, provides the detailed data necessary for the aeroacoustic model, such as radial distribution of relative wind speed, local Reynolds number and effective angle of attack.

A Blade Element Momentum (BEM) theory model was implemented (Hansen 2008), with corrections for the hub- and tip-losses and turbulent wake state. The airfoil data used in the BEM iterations are corrected for 3D effects using the stall delay model from Du and Selig (1998), with the drag adjustments from Eggers et al. (2003). The data is extrapolated using a method developed by Viterna and Janetzke (1982). The boundary layer parameters used in the noise prediction model are computed at each blade element using XFOIL viscous-inviscid interactive code (Drela 1989).

The Annual Energy Production (AEP) of the wind turbine is computed by assuming the probability density function of the wind to be a Weibull distribution (Fig. 1),

$$h\left(x;A,k\right)=\begin{cases}\frac{k}{A}\left(\frac{x}{A}\right)^{k-1}e^{-(x/A)^{k}} & x\geq 0,\\ 0 & x<0,\end{cases} \tag{1}$$

modeled using a scaling factor A and a form factor k.

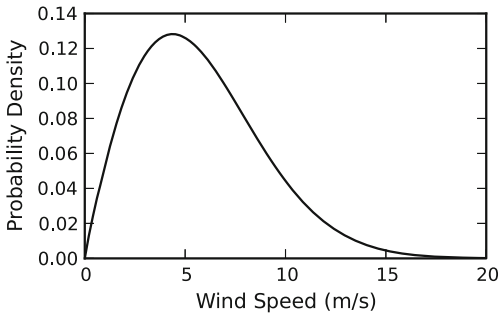

Fig. 1 Example of Weibull wind distribution curve

The AEP can then be estimated as the product of the probability function and the power curve (Hansen 2008),

$$AEP=\sum_{i=1}^{N-1}\frac{1}{2}\left(P\left(V_{i+1}\right)+P\left(V_{i}\right)\right)\times f\left(V_{i}<V_{0}<V_{i+1}\right)\times 8760, \tag{2}$$

where $P\left(V_i\right)$ is the power produced by the wind turbine at a wind speed V_i, $f\left(V_i<V_0<V_{i+1}\right)$ is the probability of the wind speed lying between V_i and V_{i+1}, and the constant term refers to the number of hours in a year.

2.2 Aeroacoustic model

The aeroacoustic prediction model implemented predicts both the turbulent inflow noise and the five mechanisms of airfoil-self noise (Wagner et al. 1996). The Sound Pressure Levels (L_p) are computed for 1/3 octave bands.

Turbulent inflow noise is predicted using the model developed by Amiet (1975) and modified by Lowson (1993). For the high frequencies, it yields

$$L^{H}_{p,\text{inflow}}=10\log_{10}\left(\frac{\rho^{2}c_{0}^{4}d}{2r_{e}^{2}}LI^{2}\frac{M^{5}\hat{k}^{3}\bar{D}}{\left(1+\hat{k}^{2}\right)^{7/3}}\right)+78.4, \tag{3}$$

where ρ is the density of air, c_0 is the speed of sound, d is the airfoil section span, L is the turbulence length scale, I is the intensity of turbulence, M is the Mach number, $\bar{D}$ denotes the effect from sound directivity, r_e is the distance from the observer and $\hat{k}=k/k_e$ is the wave number $k=2\pi f/U$ normalized by the wave number range of energy-containing eddies $k_e=3/(4L)$. U is the local inflow velocity. To account for the low frequencies, a correction factor is added to (3) leading to

$$L^{\text{flat plate}}_{p,\text{inflow}}=L^{H}_{p,\text{inflow}}+10\log_{10}\frac{K_c}{1+K_c}, \tag{4}$$

where K_c is a low frequency correction factor. This model, being based on experiments performed on a flat plate, does not account for the geometry of the airfoil, thus a correction

factor developed by Moriarty et al. (2004, 2005) is applied to (4). The total turbulent inflow noise is then obtained as

$$L_{p,\text{inflow}} = \Delta L_p + L_{p,\text{inflow}}^{\text{flat plate}} + 10, \tag{5}$$

where ΔL_p is the correction for the geometry of the airfoil and the term 10 is a correction to match with NRL data.

The turbulence intensity I in (3) is computed as a function of the surface roughness z_0 and height z as

$$I = \gamma \frac{\ln(30/z_0)}{\ln(z/z_0)}, \tag{6}$$

where

$$\gamma = 0.24 + 0.096\log_{10} z_0 + 0.016\left(\log_{10} z_0\right)^2. \tag{7}$$

Airfoil self-noise is produced when an airfoil encounters a steady non-turbulent flow field. It can be split into five mechanisms, as described by Brooks et al. (1989):

1. Turbulent boundary layer trailing edge noise,
2. Separation-stall noise,
3. Laminar boundary layer vortex shedding noise,
4. Trailing edge bluntness vortex shedding noise,
5. Tip vortex formation noise.

The 1/3 octave noise spectrum produced by the first three mechanisms can be predicted by semi-empirical scaling laws in the form

$$L_{p,i} = 10\log_{10}\left(\frac{\delta_i M^{f(i)} L \bar{D}}{r_e^2}\right) + F_i\,(\text{St}) + G_i\,(\text{Re}), \tag{8}$$

where δ_i can be either the boundary layer or displacement thickness, and $f(i)$ is a value that depends on the noise mechanism. The terms $F_i\,(\text{St})$ and $G_i\,(\text{Re})$ are spectral shape functions based on the Strouhal number and Reynolds number, respectively, which are different for each mechanism. Trailing edge bluntness vortex shedding and tip vortex formation noises are also predicted similarly, with the first using spectral shape functions based on the trailing edge solid angle Ψ_{TE} and thickness h, and the second also using a spectral shape function based on the Strouhal number.

WT rotor noise prediction The total noise produced by the WT rotor is computed by dividing the blade in n elements. The two-dimensional noise prediction is performed for each element i, resulting in

$$L_{p,i} = L_{p,\text{inflow}} + \sum_{k=1}^{5} L_{p,\text{self noise}}^{k}, \tag{9}$$

and the total sound pressure level generated by the rotor is the result of a summation of the noise from each blade element,

$$L_{p,total} = 10\log_{10}\left(\frac{N_B}{N_{az}} \sum_i 10^{\frac{L_{p,i}}{10}}\right), \tag{10}$$

where N_{az} is the number of azimuthal positions considered for noise prediction and N_B is the number of blades. The Overall Sound Pressure Level (OASPL) can be obtained by summing the noise levels at every frequency,

$$OASPL = 10\log_{10}\left(\sum_j 10^{\frac{L_{p,j}}{10}}\right), \tag{11}$$

where $L_{p,j}$ is the total noise level at frequency j.

3 Implementation

In this section, the developed aeroacoustic prediction tool is presented, followed by the description of its implementation in a Multidisciplinary Design Optimization (MDO) framework.

3.1 WT aeroacoustic prediction tool

The aerodynamic and aeroacoustic models described in the previous section were implemented using C++ and Python programming languages. The tool is robust and flexible, allowing the configuration of the simulations in detail. A representation of the tool structure is presented in Fig. 2. The following classes were implemented in Python: `Blade`, `Rotor`, `Analysis`, `Polars` and `BLayer`. The first deals with the definition of the geometry of the blade and the second, besides including an instance of a `Blade` class, also contains information about the rotor, e.g. hub height. The `Analysis` class performs the aerodynamic and aeroacoustic analyses of a given rotor. It uses the `Polars` and `BLayer` classes to obtain aerodynamic data to be used in the BEM and aeroacoustic models, which is computed by XFOIL or RFOIL (Montgomerie et al. 1997) codes. The BEM and acoustic (NOISE) models are implemented in C++ and the `Analysis` class calls them through the use of SWIG (Beazley et al. 1996), an interface compiler

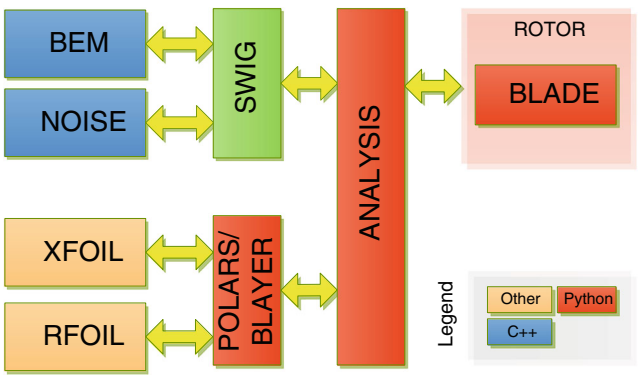

Fig. 2 Structure of the WT aeroacoustic prediction tool

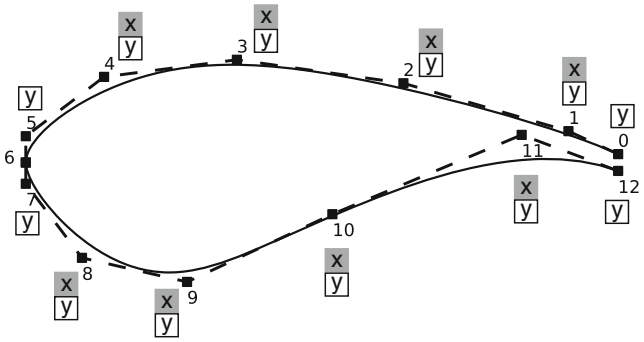

Fig. 3 NURBS airfoil parametrization control points and respective degrees of freedom

that connects programs written in C and C++ with scripting languages such as Python.

3.2 Shape parameterization

The shape of the blade was parametrized by a set of control points defining the twist and chord distributions, which were either linearly interpolated or used to construct Bézier curves, and a set of control airfoil sections.

After a survey on the most commonly used methods in airfoil shape parametrization (e.g. Hicks-Henne/Legendre Function, Spline/Bézier curves), an approach using two Non-Uniform Rational B-Splines (NURBS) curves, for the upper and lower sides of the airfoil, was chosen. NURBS curves have been used in airfoil and blade shape parametrization by Bentamy et al. (2002), Ivanović et al. (2009) and Bazilevs et al. (2011). The main advantages of this parametrization include the direct connection between the parameters and geometry, easy controllability of inflection points and local approximation (Piegl and Tiller 1997). Each of the two curves is defined by seven control points and a knot vector. The total number of degrees of freedom of the control points is 20, as schematically represented in Fig. 3. Points 0 and 12 are only allowed to move in the y-direction to ensure that the airfoil has unitary chord. In the optimization problems described in this paper, the y-coordinates of these two points are set to zero, and the Trailing Edge (TE) thickness of the airfoil, only considered in the noise prediction is assumed to be 1 % of the local chord.

This parametrization was found adequate as it was capable of accurately representing WT airfoil geometries, such as the DU 91-W2-250 airfoil (Timmer and Van Rooij 2003), as demonstrated in Fig. 4.

3.3 Optimization framework

A multi-objective optimization problem, where the values of certain objective functions f_i are to be minimized, can be stated as

$$\text{minimize } f_i(\mathbf{x}) \; i = 1, \ldots, I, \tag{12}$$

$$\begin{aligned} \text{subject to } & g_m(\mathbf{x}) \leq 0, \qquad m = 1, \ldots, M, \\ & h_n(\mathbf{x}) = 0, \qquad n = 1, \ldots, N, \\ & x_k^L < x_k < x_k^U, \; k = 1, \ldots, K, \end{aligned} \tag{13}$$

where $\mathbf{x}$ is the vector of design variables, and g_m and h_n are the inequality and equality constraints, respectively. Possible objective functions would be the AEP and OASPL values of a wind turbine.

A MDO framework was developed using the Python module *pyOpt* (Perez et al. 2012) as the optimizer and the previously described WT aeroacoustic prediction tool and geometry parametrization modules. Their connectivity is illustrated in Fig. 5.

The Non-dominated Sorting Genetic Algorithm NSGA-II (Deb et al. 2002) was chosen as the optimization algorithm, since it solves non-convex, non-smooth single and multi-objective problems. NSGA-II has been used in the optimization of wind turbine blades by Petrone et al. (2011) and Wang et al. (2011). The GA parameters used in the optimization are presented in Table 1. They are the probability

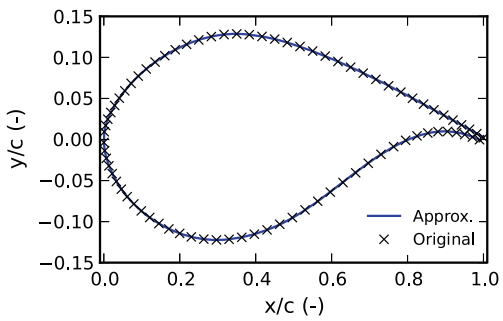

Fig. 4 Approximation of the DU 91-W2-250 airfoil shape using the NURBS curves parametrization

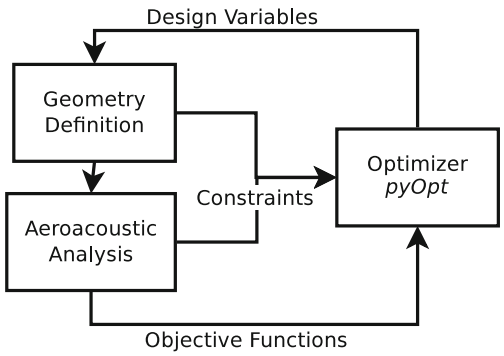

Fig. 5 Flowchart of the optimization framework

Table 1 GA parameters used in the optimization

Parameter	Value
P(Crossover)	0.6
P(Mutation)	0.2
η_c	10.0
η_m	20.0
Seed	0.0

of occurrence of crossover and mutation and distribution indexes for the same two operations.

A convergence study was performed to gain insight of the minimum population size and number of generations required to obtain a converged solution. The optimization problem consisted in maximizing the AEP produced by the blade of the NREL Phase II (a rectangular and untwisted bladed wind turbine) (Simms et al. 1999) by varying its twist and chord. The twist was defined by a Bézier curve with four control points, similarly to what is schematically represented in Fig. 10, which resulted in six design variables. The chord was varied linearly along the blade with two control points, defined at the hub and tip of the blade. As such, a total of eight design variables were considered. The evolution of the fitness (best AEP of the population) throughout the optimization is presented in Fig. 6. It can be seen that with a population size of 64 individuals, the optimization converges in about 50 fewer generations than with a population of 8 individuals, with the difference between the two optimal solutions being less than 1 %. However, this lower number of generations required to achieve convergence does not mean a faster optimization, as the number of function calls per generation is equal to the population size. Based on this and other results, it was concluded that a population size between n and $2n$, with n being the number of design variables, is able to provide an accurate solution while maintaining the computational costs of the optimization low.

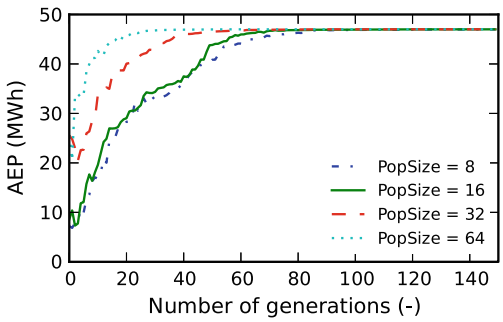

Fig. 6 Evolution of the fitness of the population of an optimization case with 8 design variables (twist + chord)

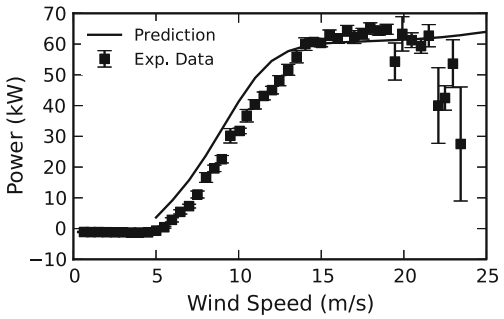

Fig. 7 AOC 15/50 predicted and measured power curve (Measurements from Jacobson et al. 2003)

3.4 Validation of the aeroacoustic prediction code

The AOC 15/50 is a downwind, three bladed turbine with a rated power of 50 kW and a blade length of 7.5 m (Seaforth Energy 2010). It uses the NREL S821, S819 and S820 profiles, defined at 40, 75 and 95 % of the blade span, respectively. The measured and predicted power curves are presented in Fig. 7, where slight over-prediction can be observed up to a wind speed of approximately 14 m s^{-1}. After that, the numerical model slightly under-predicts the maximum power generated and fails to predict the loss in power due to stall. This is a known limitation of the BEM model and its implications are minimized by choosing operation conditions where stall does not occur.

In Fig. 8, the predicted noise spectrum of the wind turbine is presented, along with measured data, at a wind speed of 8 m s^{-1}, and the difference between the predicted and measured data. The simulation was performed assuming a TE bluntness of 1 % of the chord and a TE angle of 6°. All noise mechanisms described in Section 2.2 were considered and the observer is located at ground level, 32.5 m downwind of the turbine (in the direction aligned with the turbine rotation axis). Although it is not able to predict the peak below 1 kHz (with an absolute error of about −12 dB(A)) and underpredicting the noise levels above 2 kHz (frequency at which the absolute error is about 6 dB(A)), the prediction tool can

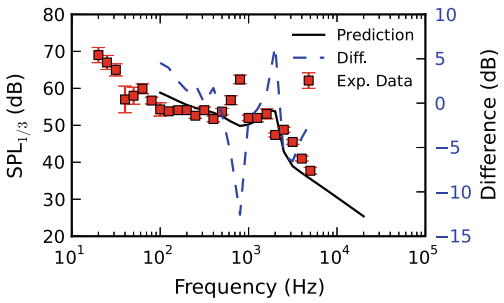

Fig. 8 AOC 15/50 overall sound pressure level measurement and prediction data at wind speeds of 8 m s^{-1} (Measurements from Ref. Huskey et al. 1999)

be said to provide good qualitative results, sufficient for the conceptual design framework that it is intended for.

4 Results

In this section, the results of two optimization cases performed on the AOC 15/50 blade are presented. The multi-objective optimization problems aimed the simultaneous maximization of the annual energy production and the minimization of the overall noise produced by the wind turbine.

The simulations were performed assuming a wind distribution represented by a Weibull curve with parameters $A = 6.48\ \mathrm{m\,s^{-1}}$ and $k = 1.99$, presented in Fig. 9. These parameters represent the wind distribution in the Portuguese municipality of Vila do Bispo, in the southwest of Portugal (Costa 2004).

The performance of the turbine was predicted for wind speeds ranging from $4\ \mathrm{m\,s^{-1}}$ to $25\ \mathrm{m\,s^{-1}}$, in $1\ \mathrm{m\,s^{-1}}$ intervals and the noise was computed assuming the observer at ground level, 96 m (three times the height of the tip of the blade at its higher position) downwind of the turbine, in the direction of its rotation axis. The ground roughness was taken as 0.5 m, corresponding to a type of terrain with many bushes and obstacles. Both boundary layer parameters and airfoil polar data were computed using XFOIL. The TE was assumed to have a thickness of 1 % of the chord and a constant angle of 6°. Due to the non-aerodynamic shape of the sections up to 40 % of the blade span, the noise was only computed in the 60 % outer part.

The shape of the blade was defined by four control sections (see Fig. 10), being the first at the hub considered frozen as a circle. At each of the other three sections, the coordinates of 10 control points were used as design variables (the y-coordinates of control points 0 and 12 were kept constant see Fig. 3), resulting in a total of 54 variables (18 per control section).

The twist was defined using a 5th-order Bézier curve, resulting in 6 design variables. The chord was defined by

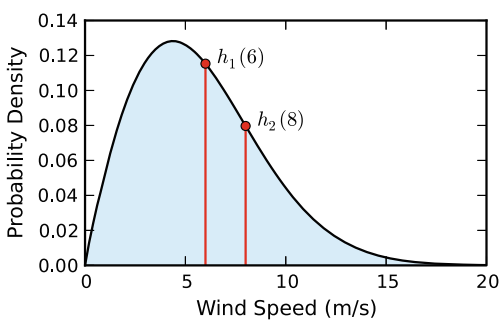

Fig. 9 Weibull wind distribution used in the optimization

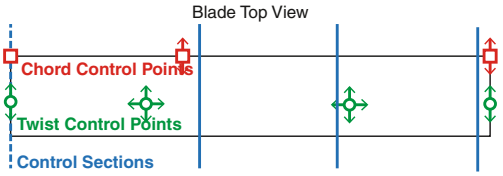

Fig. 10 Blade control sections and design variables used in the optimization

linear interpolation of 3 control points being the first fixed at the hub, resulting in 2 design variables. This resulted in a total of 62 design variables. The initial variable values are presented in Fig. 11.

The search space of the control section variables was defined as ±10 % in the x-direction and ±30 % in the y-direction, relative to the initial control points. The search space of the chord variables was defined as the initial chord values minus 0.3 m and plus 0.6 m. The twist values were allowed to vary from −15 to 15°. This defined the lower and upper bounds of te vector of design variables $\mathbf{x}^L$ and $\mathbf{x}^U$ respectively.

The optimization was subject to a set of constraints to impose feasible geometries. The first set regards the chord and twist distributions and imposes a reduction of their values towards the tip of the blade (excluding the root chord). This can be expressed as

$$z_i^{\text{twist or chord}} \leq z_{i+1}^{\text{twist or chord}} \tag{14}$$

and

$$y_i^{\text{twist or chord}} \geq y_{i+1}^{\text{twist or chord}}. \tag{15}$$

The control points of each control section j were also subject to a set of constraints to ensure that they would not cross each other,

$$\begin{aligned} x_i^{cp,j} &\geq x_{i+1}^{cp,j}, \quad \text{on the upper curve} \\ x_i^{cp,j} &\leq x_{i+1}^{cp,j}, \quad \text{on the lower curve} \end{aligned} \tag{16}$$

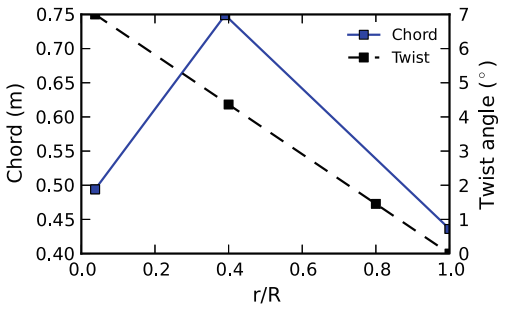

Fig. 11 Initial twist and chord control points and resulting distributions

and to avoid unwanted inflections on the upper and lower curves:

$$y_3^{cp,j} \geq y_4^{cp,j} + \left(y_2^{cp,j} - y_4^{cp,j}\right) \frac{x_3^{cp,j} - x_4^{cp}}{x_2^{cp,j} - x_4^{cp,j}}, \tag{17}$$

$$y_9^{cp,j} \leq y_8^{cp,j} + \left(y_{10}^{cp,j} - y_8^{cp,j}\right) \frac{x_9^{cp,j} - x_8^{cp,j}}{x_{10}^{cp,j} - x_8^{cp,j}}. \tag{18}$$

The two optimization cases differ from each other in the computation of the noise generated by the turbine. In the first one, the noise was predicted for a wind speed of 6 $\mathrm{m\,s^{-1}}$, which is the closest to the average wind speed of the selected site. In the second case, the noise was predicted for wind speeds of 6 and 8 $\mathrm{m\,s^{-1}}$, by averaging the OASPL for each wind speed. These two optimization cases correspond to single-operating and multi-operating point conditions, respectively, and can be posed in standard form as

$$\begin{aligned} &\text{minimize} \quad f_1(\mathbf{x}) = -AEP \\ &\quad \text{and} \quad f_2(\mathbf{x}) = OASPL, \end{aligned} \tag{19}$$

$$\begin{aligned} &\text{subject to} \quad \mathbf{g}(\mathbf{x}) \leq 0, \\ &\qquad \mathbf{x}^L < \mathbf{x} < \mathbf{x}^U, \end{aligned} \tag{20}$$

where $\mathbf{g}$ is a set of 56 constraints, given by (14), (15), (16), (17) and (18).

From the results of the optimization described in Section 3.3, the population used in the two optimization cases contained 68 individuals. The first optimization case was allowed to run for 140 generations and the second, due to the increased computational cost and time constraints, was only allowed to run for 70 generations.

4.1 Single Operating Point Optimization

The Single Operating Point (SOP) optimization resulted in the Pareto front presented in Fig. 12, where the evolution of the population of solutions throughout the GA generations run can also be visualized.

Three solutions selected from the final population are presented in Fig. 13. They represent the ones that produces

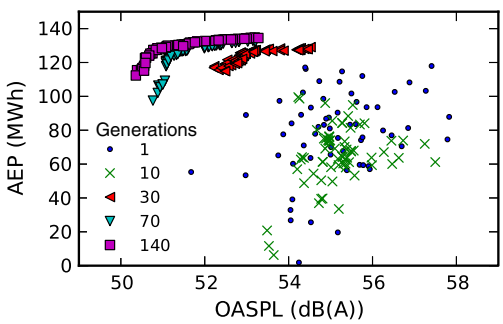

Fig. 12 Evolution of the population during the SOP optimization

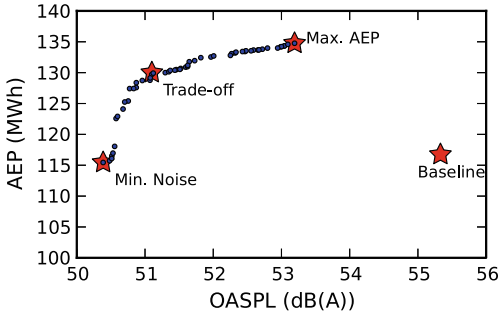

Fig. 13 Pareto front for the SOP optimization

the lowest noise levels (Min. Noise), the higher value of AEP (Max. AEP) and a trade-off between the previous two.

The geometry of each of the three selected solutions is presented in Fig. 14, along with a contour of the noise generated in the blade.

The chord and twist distributions of these selected solutions are presented in Figs. 15 and 16, respectively.

The differences between the three solutions are visible, as are the differences in the shape of the blade. The maximum AEP geometry shows a much higher tapper towards the tip of the blade than the other two solutions. This contradicts the expectations, as the noise is produced mainly near the tip and is proportional to the chord of the blade. A possible explanation is the reduced loading of the blade due to the cross-sectional shape of the airfoils near the tip.

The profiles of the three active control sections for the three selected solutions are presented in Fig. 17. The initial airfoil shape is shown in dashed lines. At 40 % of the blade, there is a slight increase in camber, specially in the trade-off and maximum AEP geometries and in the front part of the airfoil. This increase in camber is also visible at 75 % of the blade, again for the trade-off and maximum AEP geometries, while the minimum noise airfoil presents a slight decrease in camber. At this station, a decrease in airfoil thickness is also visible for all the three geometries.

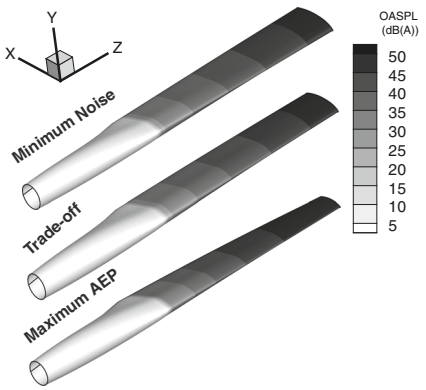

Fig. 14 Comparison of the three selected optimal blade geometries of the SOP optimization

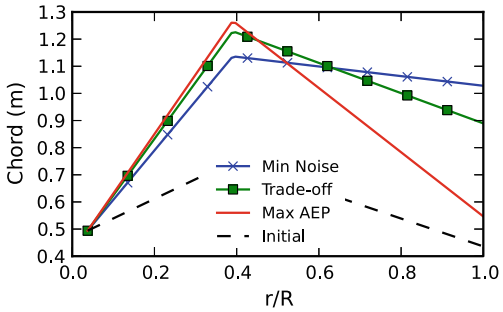

Fig. 15 Chord distribution of optimized AOC 15/50 blades for the SOP optimization

The optimal airfoil shapes of the section located at 95 % of the blade are very similar to each other and both present an increase in camber.

Figure 18 presents the difference of noise generated by the blades in the rotor plane between the baseline and the three selected Pareto solutions. The non-symmetric behavior is visible as the noise levels are higher in between 90° and 180°, corresponding to the blade downward movement. This is due to the observer not being located in the axial axis of the turbine. The minimum noise and trade-off solutions present lower noise levels in the majority of the rotor plane, and the maximum AEP solution, although presenting some regions with a higher generation of noise, also produces lower noise levels in the outer region of the blade when compared to the baseline blade.

In Fig. 19, the distribution of the power produced by the initial and the three optimized blades is presented for the turbine operating at a wind speed of 6 m s^{-1}. There is an overall decrease in the loading of the blade, which can also be seen in Fig. 20, where the aerodynamic power generated by the turbine as a function of wind speed is presented. At 6 m s^{-1}, the power production of the optimized blades is lower than the initial – a result of the reduction of the noise emission levels. However, the AEP values are kept higher than the initial ones due to the higher power production for wind speeds of 10 m s^{-1} and above (as seen in the Weibull curve of Fig. 9, the main contribution to the AEP is between 0 and 15 m s^{-1}).

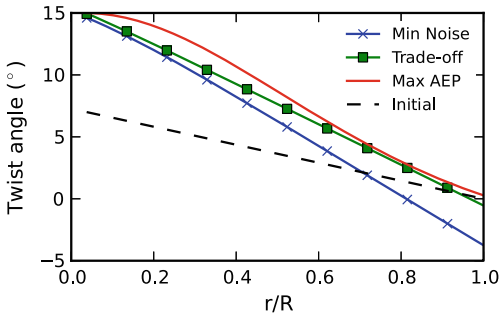

Fig. 16 Twist distribution of optimized AOC 15/50 blades for the SOP optimization

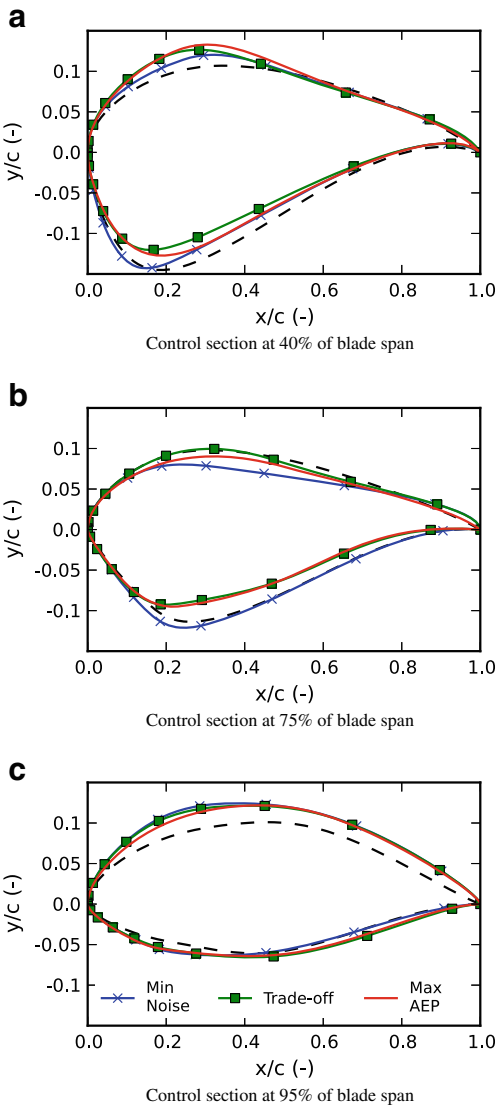

Fig. 17 Initial and optimized airfoil shapes for the SOP optimization

4.2 Sensitivity analysis of the SOP case

The sensitivity of the functions of interest to the design variables was investigated for the trade-off solution of the SOP optimization case. The derivatives are presented in graphical form in Figs. 21 and 22, where the vectors represent the direction where the control points of each section should move to either increase the AEP or decrease the OASPL, respectively. It is visible from the figures that the functions of interest are much more sensitive to the shape of the control sections closer to the tip of the blade (note the different scales of the plots). This is an expected result, as

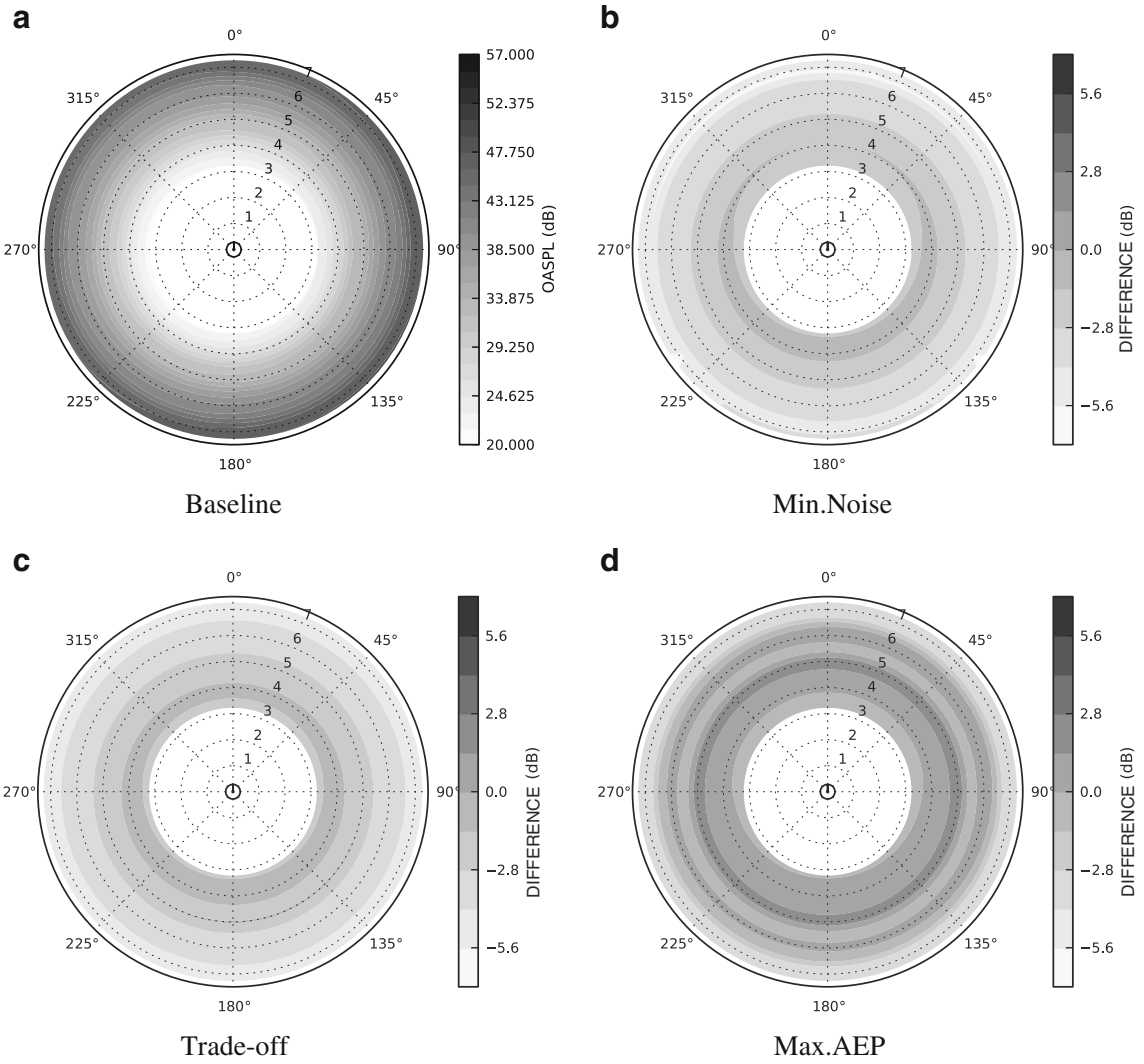

Fig. 18 Differences in overall sound pressure level across the rotor for the three selected optimal blade geometries of the SOP optimization case, using the baseline blade as reference

the outer part of the blade is where the majority of the torque and noise is produced. The compromise between noise and energy production is also visible on the sensitivity of control points 4 and 8 (among others), whose derivatives differ in sign of their x-component (between the AEP and OASPL sensitivities). At the inner section, an increase in

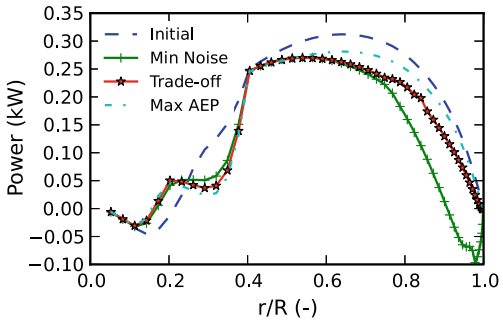

Fig. 19 Local power distribution on initial and optimized blades for the SOP optimization

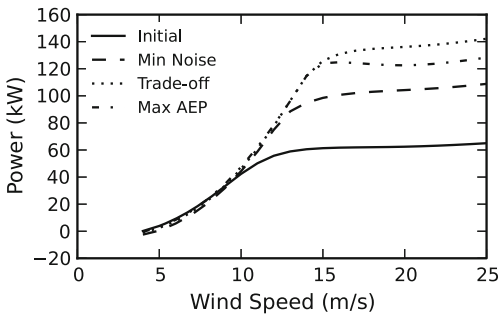

Fig. 20 Initial and optimized power curves for the SOP optimization

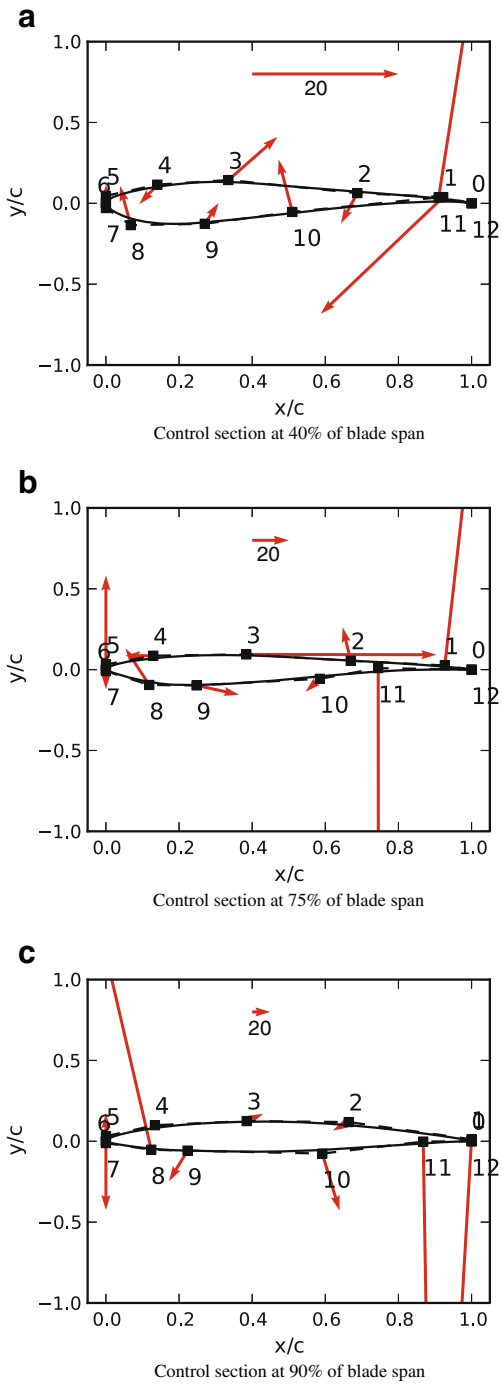

Fig. 21 Sensitivity of AEP with respect to the cross-section shape control points of the SOP optimization

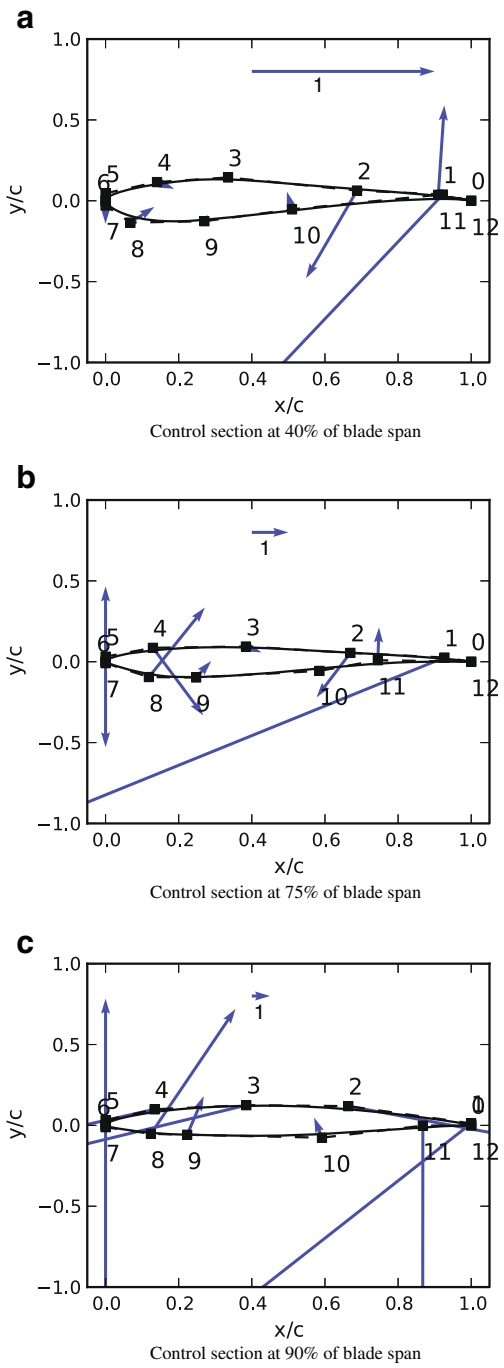

Fig. 22 Sensitivity of OASPL with respect to the cross-section shape control points of the SOP optimization

aft loading (point 11 going up and right and point 1 going left and down) would both increase the AEP and reduce the OASPL, which is in conformance with the results presented in Fig. 17. At the other two sections, both the AEP and OASPL present a large sensitivity to the position of these two points, indicating that the aft part of the blade is very important to the aeroacoustic performance of the turbine.

4.3 Multi operating point optimization

The previous optimization case only considered the noise generated at a particular wind speed. With the aim of obtaining a blade geometry better fitted for a wider operating range, representing a multi-operating point (MOP) case, many more wind speeds need to be considered in the computation of the OASPL. As this would result in much higher

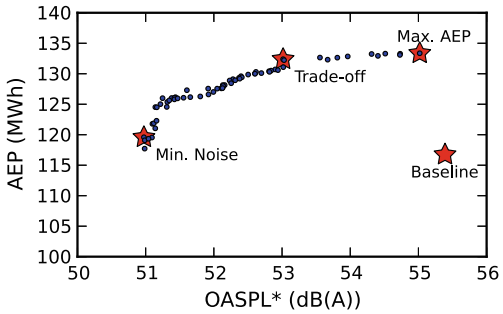

Fig. 23 Pareto front for the MOP optimization

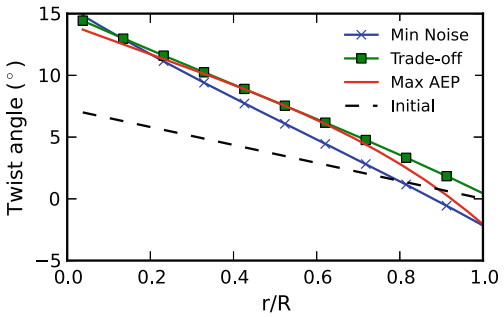

Fig. 25 Twist distribution of optimized AOC 15/50 blades for the MOP optimization

computational cost, only one more wind speed was considered and the noise was computed for wind speeds of 6 and 8 $\mathrm{m\,s^{-1}}$. The objective function relative to the noise is a weighted average of the OASPL at different speeds, defined as

$$f_2 = \frac{10\log_{10}\sum_{i=1}^{n} h_i 10^{OASPL_i/10}}{\sum_{i=1}^{n} h_i}, \tag{21}$$

where h_i are weight factors based on the Weibull distribution of the wind speed (see Fig. 9). All other operating conditions of the turbine were the same as the previous optimization case.

The Pareto front obtained in this case is presented in Fig. 23, where, similarly to the SOP case, three optimal solutions are highlighted.

The chord and twist distributions of the three highlighted solutions are presented in Figs. 24 and 25, respectively. It can be seen that, similarly to the previous case, the maximum AEP blade has a much greater tapper than the other two blades. This is probably due to the fact that the optimizer uses the control section profiles, which have a stronger input on power and noise, to meed the goals.

The profiles of the three active control sections at 40, 75 and 95 % of the blade span, for the three selected solutions, are presented in Fig. 26. As reference, the initial shapes are shown in dashed lines. Starting with the section at 40 % span, it is visible that the trade-off geometry is much more similar to the maximum AEP than to the minimum noise.

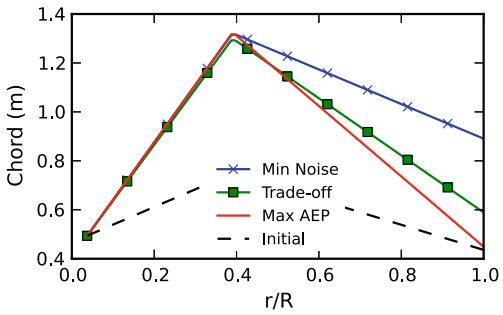

Fig. 24 Chord distribution of optimized AOC 15/50 blades for the MOP optimization

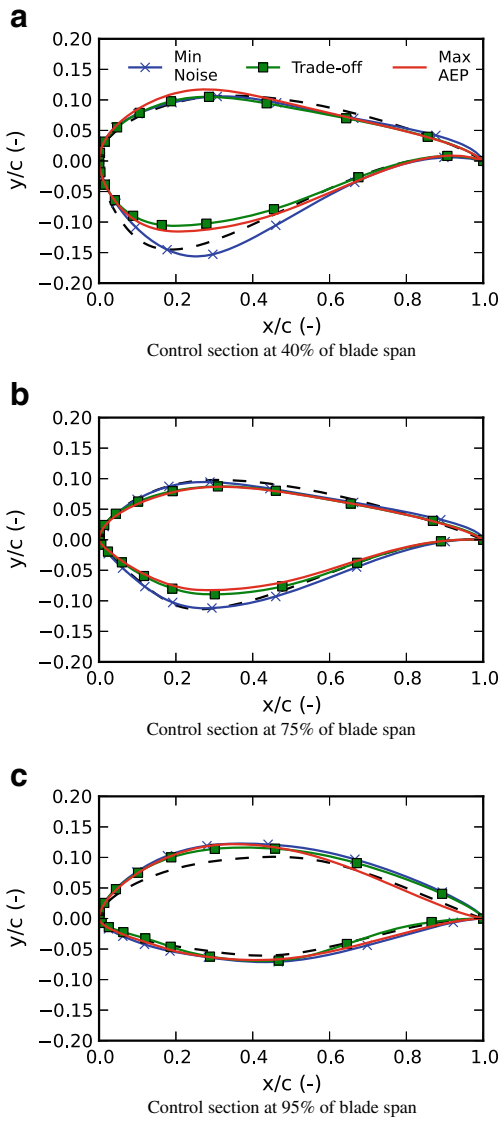

Fig. 26 Initial and optimized airfoil shapes for the MOP optimization

Table 2 Optimized AEP and OASPL values obtained in the SOP and MOP optimization cases

		AEP [MWh]		OASPL [dB(A)]	
SOP	Baseline	116.74		55.33	
	Min Noise	115.45	−1 %	50.38	−9.8 %
	Max AEP	134.76	15 %	53.19	−4 %
MOP	Baseline	116.74		55.39	
	Min Noise	119.58	2 %	50.97	−8 %
	Max AEP	133.36	14 %	55.02	−1 %

The first two present a reduced thickness, compared to the original shape, while the minimum noise airfoil presents a higher maximum thickness. At 75 % span, the same as described previously is also observed, with the exception that the minimum noise airfoil does not exhibit a maximum thickness to chord ratio (t/c) higher than the initial airfoil. In the last section, at 95 % span, the trade-off solution is more similar to the minimum noise, particularly for $x/c > 0.6$, where, in these two solutions, the upper surface is much higher than the original. This fact probably occurs due to the noise being mainly generated in the outer part of the blade. For $x/c < 0.6$ the shape of the three solutions is very similar, with a t/c higher than the initial airfoil shape.

4.4 Comparison between optimal SOP and MOP blades

Table 2 presents the AEP and OASPL values of the optimal blades selected in the previous sections, as well as the baseline configuration.

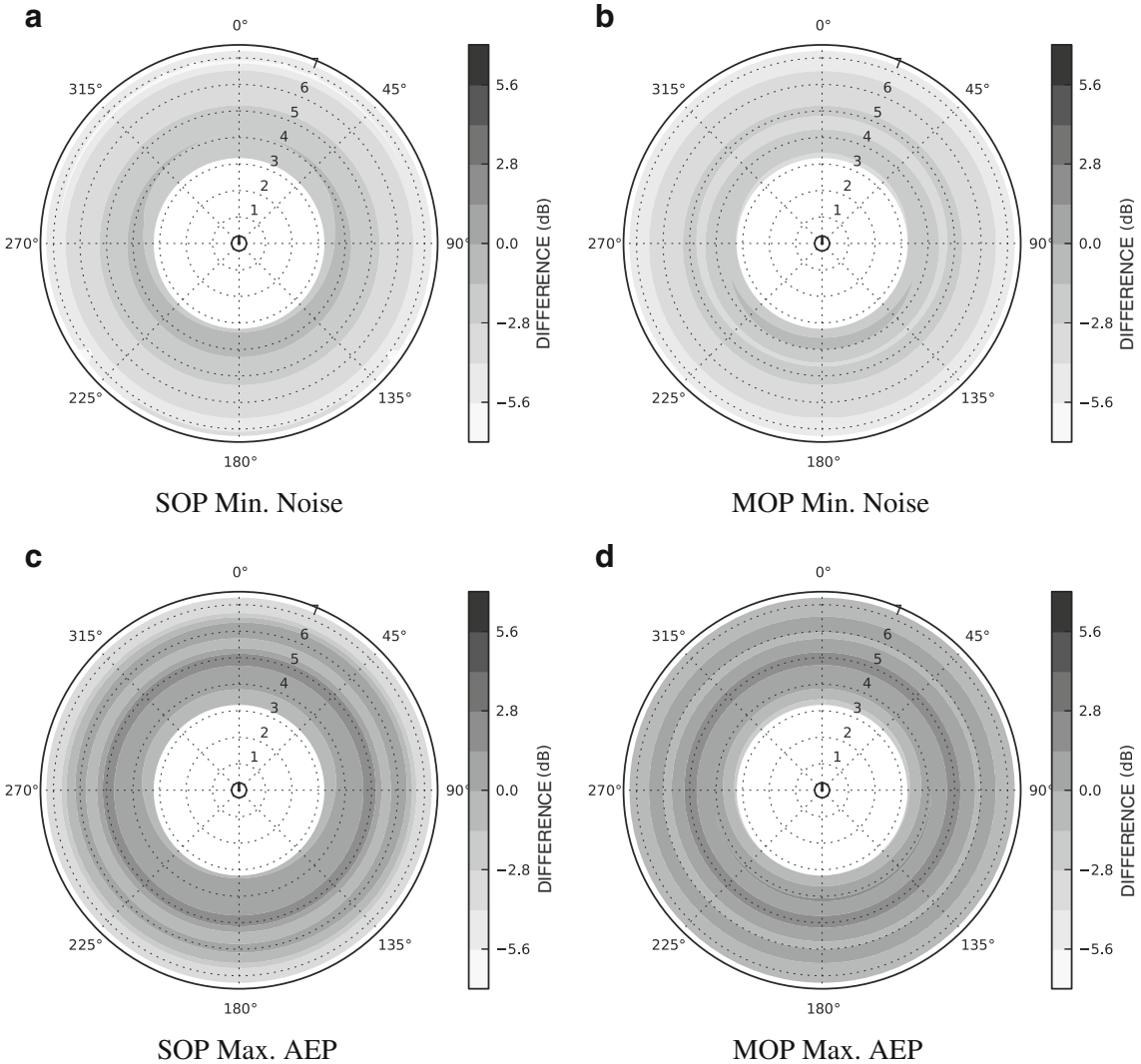

Fig. 27 Differences in overall sound pressure level across the rotor for selected optimal blade geometries of the SOP and MOP optimization cases, using the baseline blade as reference

The SOP case presents better results (lower OASPL and higher AEP values), specially for the maximum AEP blades, when compared to the MOP case. This is due to the MOP case taking into account higher operating wind speeds when computing the OASPL (21).

In the minimum noise solution, in the SOP case, a maximum reduction of 9.8 % of noise levels was achieved, along with a 1 % reduction of the AEP, whereas, the MOP case was able to reduce the OASPL in 8 % and still increase the AEP by 2 %.

Comparing the two maximum AEP solutions, the SOP optimization resulted in an increase of AEP by 15 % and a reduction of OASPL by 4 %. The MOP optimization achieved similar results regarding the AEP value, with an increase of 14 %, while still achieving a marginal noise reduction of 1 %.

These results can also be observed in Fig. 27, where the differences in OASPL across the rotor between the baselines and the optimal solutions are presented.

The chord and twist distributions of the minimum noise and maximum AEP blades of both the SOP and MOP cases are presented in Fig. 28. The minimum noise geometry of the two optimization cases differ from each other quite significantly. At $r/R = 0.4$, while the MOP blade presents the higher chord value of the solutions presented, the SOP has the lowest. At the tip of the blade, the situation is different, and the SOP case blade presents a higher chord value than the MOP. Comparing the maximum AEP geometries of both cases, the differences are not as evident as for the minimum noise blades. Although the inversion previously described also exists (with the MOP case having a higher chord value at $r/R = 0.4$ than the SOP, and lower at the tip), the chord distributions are very similar. Regarding the twist distribution, the inverse occurs between the SOP and MOP cases. In the minimum noise blades, the twist angle varies almost linearly along the blade for the two optimization cases, with the MOP blade twist angle being always slightly larger. In the maximum AEP blade, the twist distributions are not as similar and, with the exception at $r/R \approx 0.7$ where the two blades have the same twist angle, the MOP blade presents slightly lower twist angles.

The airfoil shapes at 75 % and 95 % span of the blades presented in Fig. 28 can be seen in Fig. 29. At $r/R = 0.75$, it is noticeable that the maximum AEP airfoils have a lower t/c ratio when compared to the minimum noise airfoils. It can also be seen that the minimum noise airfoil obtained from the SOP case has a lower t/c than the one obtained from the MOP case, specially at $x/c \approx 0.4$. The airfoil shapes at $r/R = 0.95$ are all very similar to each other, except for the maximum AEP (MOP) one, that does not have the increased camber in its aft part as all the others have. In general, at this outer station, the optimized airfoils present an increase in t/c and camber.

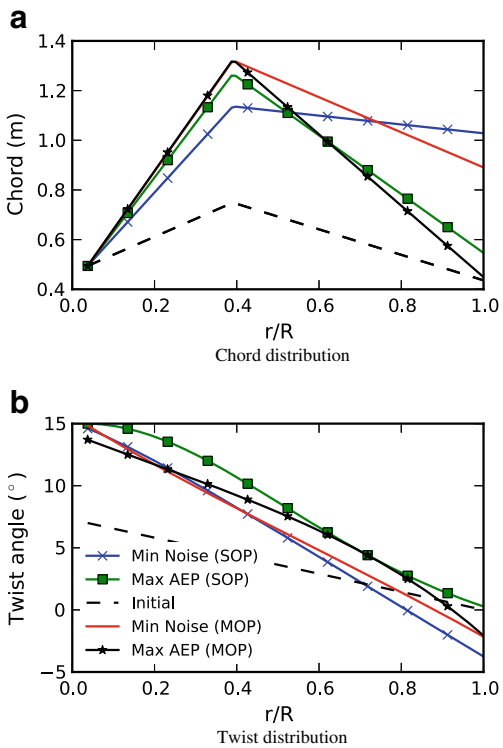

Fig. 28 Optimized AOC 15/50 blades for SOP and MOP optimization cases

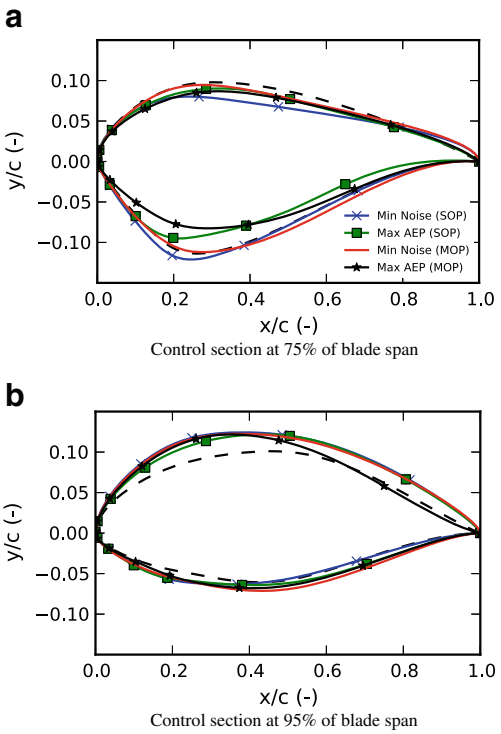

Fig. 29 Initial and optimized airfoil shapes for the SOP and MOP optimization cases

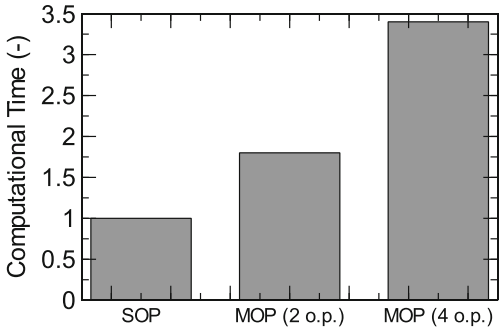

Fig. 30 Comparison of the computational time between SOP and MOP optimization cases

The comparison of computational time required between the SOP and MOP cases is presented in Fig. 30, along with an extrapolation for the case of MOP with four operating points. The MOP case requires about 1.8 times the computational time of the SOP case. A value below but close to 2 was expected, as the only extra computations executed in the MOP case, compared to the SOP one, are the ones related to the aeroacoustic analysis (the aerodynamic analysis remains as it already takes into account a set of operating conditions). Even so, the aeroacoustic analysis are the most computational demanding, thus, increasing the operating points would greatly increase the computational time. For a given number of operating points, n, the time required would be k times larger than for the SOP case. From a linear fit of the data presented in Fig. 30, k can be approximated as $k \approx 0.8n + 0.2$.

5 Conclusions

The preliminary aeroacoustic design of WT blades to address maximum noise emission regulations was successfully achieved. By altering an initial blade geometry, the developed WT optimization framework was able to find a set of optimal blade shapes that minimized noise emission while maintaining, to some extent, their aerodynamic performance.

Low-fidelity WT aerodynamic and aeroacoustic prediction models were successfully implemented and validated against experimental data. A geometrical model of the wind turbine blade was also developed, that used NURBS and Bézier curves for the definition of the cross sectional airfoil shapes and twist and chord distributions, respectively. The NURBS parametrization proved to be able to reproduce various different airfoil shapes commonly used in wind turbines. These modules were successfully implemented into an optimization framework, that demonstrated being able to produce optimal solutions in the various performed test cases.

Nowadays, tools like the developed framework should be used in the design phase of any wind turbine to increase its performance to the maximum possible extent. As the geometries of the blades are already highly manually tuned by the designers, the use of such automatic tools might give the wind turbine manufacturers a competitive edge. The relative small computational requirement of each optimization is a key factor, as it allows for a greater diversity of geometries and configurations to be analyzed, thus increasing the probability of obtaining an overall better solution.

The design of after market blades to conform to site specific noise regulations is also a possibility, where the installed blades already have a specific geometry and the only option is to add material, to change the its shape. This is envisioned through the use of skins made of composite materials that can be glued to the outer surface using structural adhesives. The developed design framework can be easily adapted to address this specific problem.

References

Amiet R (1975) Acoustic radiation from an airfoil in a turbulent stream. J Sound Vib 41(4):407–420

Bazilevs Y, Hsu MC, Akkerman I, Wright S, Takizawa K, Henicke B, Spielman T, Tezduyar TE (2011) 3D simulation of wind turbine rotors at full scale. Part I: geometry modeling and aerodynamics. Int J Numer Methods Fluids 65(1–3):207–235

Beazley DM et al (1996) SWIG: an easy to use tool for integrating scripting languages with C and C++. In: Proceedings of the 4th USENIX Tcl/Tk workshop, pp 129–139

Bentamy A, Trépanier JY, Guibault F (2002) Wing shape optimization using a constrained nurbs surface geometrical representation. In: ICAS congress

Bizzarrini N, Grasso F, Coiro D (2011) Numerical optimization for high efficiency, low noise airfoils

Brooks T, Pope D, Marcolini M (1989) Airfoil self-noise and prediction, vol 1218. National Aeronautics and Space Administration, USA

Coimbra JFG (2012) Aero-acoustic optimization of airfoils for wind turbines. Master's thesis, Instituto Superior Técnico

Colby W, Dobie R, Leventhall G, Lipscomb D, McCunney R, Seilo M, Søndergaard B (2009) Wind turbine sound and health effects. An expert panel review. American Wind Energy Association

Costa P (2004) Atlas do potencial eólico para Portugal continental. Master's thesis, Faculdade de Ciências da Universidade de Lisboa, Lisboa

Deb K, Pratap A, Agarwal S, Meyarivan T (2002) A fast and elitist multiobjective genetic algorithm: NSGA-II. IEEE Trans Evol Comput 6(2):182–197

Drela M (1989) XFOIL—an analysis and design system for low Reynolds number airfoils. Low Reynolds number aerodynamics

Du Z, Selig M (1998) A 3-d stall-delay model for horizontal axis wind turbine performance prediction. In: Proceedings of the 1998 ASME wind energy symposium. Reno, pp 9–19

Eggers AJ, Chaney K, Digumarthi R (2003) An assessment of approximate modeling of aerodynamic loads on the UAE rotor. ASME

Göçmen T, Özerdem B (2012) Airfoil optimization for noise emission problem and aerodynamic performance criterion on small scale wind turbines. Energy

Hansen M (2008) Aerodynamics of wind turbines. Earthscan, London Sterling

Huskey A, Link H, Butterfield C (1999) Wind turbine generator system acoustic noise test report for the AOC 15/50 wind turbine. Tech. rep., AOC1550-CA-99182-1000. National Renewable Energy Laboratory, Golden

Ivanović I, Petrović Z, Stupar S (2009) Helicopter rotor blade shape optimization using NURBS for airfoil shape parameterization. In: AIP conference proceedings, vol 1168, p 131

Jacobson R, Meadors E, Link H (2003) Power performance test report for the AOC 15/50 wind turbine, test b in golden, colorado. United States Department of Energy by National Wind Technology Centre National Renewable Energy Laboratorys, pp 1–150

Leloudas G (2006) Optimization of wind turbines with respect to noise

Lowson M (1993) Assessment and prediction of wind turbine noise. Energy Technology Support Unit

Montgomerie BOG, Brand AJ, Bosschers J, van Rooij RPJOM (1997) Three-dimensional effects in stall. Tech. rep., Energy Research Center of the Netherlands

Moriarty P, Guidati G, Migliore P (2004) Recent improvement of a semi-empirical aeroacoustic prediction code for wind turbines. In: Proceedings of 10th AIAA/CEAS aeroacoustics conference. Manchester

Moriarty P, Guidati G, Migliore P (2005) Prediction of turbulent inflow and trailing-edge noise for wind turbines. In: 11th AIAA/CEAS aeroacoustics conference (26th Aeroacoustics conference), pp 1–16

Pedersen E, Waye KP (2004) Perception and annoyance due to wind turbine noise-a dose-response relationship. J Acous Soc Am 116(6), pp 3460–3470

Perez RE, Jansen PW, Martins JRRA (2012) pyOpt: a python-based object-oriented framework for nonlinear constrained optimization. Struct Multidiscip Optim 45(1):101–118. doi:10.1007/s00158-011-0666-3

Petrone G, de Nicola C, Quagliarella D, Witteveen J, Axerio-Cilies J, Iaccarino G (2011) Wind turbine optimization under uncertainty with high performance computing. In: 41st AIAA fluid dynamics conference. Honolulu

Piegl LA, Tiller W (1997) The NURBS book. Springer, New York

Schepers JG, Curvers A, Oerlemans S, Braun K, Lutz T, Herrig A, Wuerz W, Mantesanz A, Garcillan L, Fischer M et al (2007) Sirocco: silent rotors by acoustic optimisation. In: Second international meeting on wind turbine noise

Seaforth Energy (2010) AOC 15/50 Specification Sheet. http://seaforthenergy.com/wp-content/uploads/2010/12/AOC1550-Specification-Sheet.pdf

Simms DA, Hand MM, Fingersh LJ, Jager DW (1999) Unsteady aerodynamics experiment phases II-IV test configurations and available data campaigns. doi:10.2172/12144

Stephens DG, Shepherd K, Hubbard H, Grosveld F (1982) Guide to the evaluation of human exposure to noise from large wind turbines. NASA TM 83288

Timmer W, Van Rooij R (2003) Summary of the delft university wind turbine dedicated airfoils. J Solar Energy Eng 125(4):488–496

Viterna L, Janetzke D (1982) Theoretical and experimental power from large horizontal-axis wind turbines. U.S. Department of Energy, Conservation and Renewable Energy Wind Energy Technology Division

Wagner S, Bareiss R, Guidati G (1996) Wind turbine noise. Springer, Berlin

Wang L, Wang T, Luo Y (2011) Improved non-dominated sorting genetic algorithm (NSGA)-II in multi-objective optimization studies of wind turbine blades. Appl Math Mech 32(6):739–748